

# Spectral Engineering of InSe Nanobelts for Full-Color Imaging by Tailoring the Thickness

Chun-Yan Wu,\* Kai-Jun Cao, Yu-Xuan Le, Jing-Yue Li, Chen-Yue Zhu, Li Wang, Yu-Xue Zhou, Di Wu, and Lin-Bao Luo\*



Cite This: *J. Phys. Chem. Lett.* 2022, 13, 2668–2673



Read Online

ACCESS |



Metrics & More

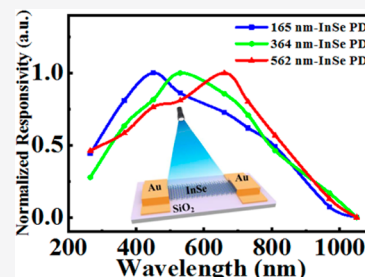


Article Recommendations



Supporting Information

**ABSTRACT:** In this work, we report on the synthesis of InSe nanobelts through a catalyst-free chemical vapor deposition (CVD) growth approach. A remarkable blue shift of the peak photoresponse was observed when the thickness of the InSe nanobelt decreases from 562 to 165 nm. Silvaco Technology Computer Aided Design (TCAD) simulation reveals that such a shift in spectral response should be ascribed to the wavelength-dependent absorption coefficient of InSe, for which incident light with shorter wavelengths will be absorbed near the surface, while light with longer wavelengths will have a greater penetration depth, leading to a red shift of the absorption edge for thicker nanobelt devices. Considering the above theory, three kinds of photodetectors sensitive to blue (450 nm), green (530 nm), and red (660 nm) incident light were achieved by tailoring the thickness of the nanobelts, which can enable the spectral reconstruction of a purple “H” pattern, suggesting the potential application of 2D layered semiconductors in full-color imaging.



Two-dimensional (2D) layered semiconductors have emerged as the most promising material candidates for next-generation electronic and optoelectronic devices because of their unique structures and physical properties.<sup>1–3</sup> Unlike bulk or thin-film materials, the atoms in 2D layered semiconductors are held together by strong in-plane covalent or ionic bonds while the atomic layers are stacked in the out-of-plane direction with weak van der Waals interactions, which facilitates the fabrication of thinner sheets and the extraction of few-layer or even monolayer nanosheets exfoliated from their parent bulk crystals.<sup>4,5</sup> In addition, the unique layered structure also results in intriguing merits, including high carrier mobility, strong light–matter interactions, and layer-dependent electronic and optical properties.<sup>6–8</sup>

Indium selenide (InSe), a typical 2D layered semiconductor with a direct bulk band gap of 1.25 eV, has been widely explored in fields of high-performance broadband photodetection.<sup>9–12</sup> For instance, Tamalampudi et al. have demonstrated the broadband photodetection of few-layered InSe photodetectors for the visible to near-infrared (NIR) region (450–785 nm). The responsivity increased with the decrease of the wavelength and reached 12.3 A/W at 450 nm.<sup>13</sup> Ajayan et al. have reported an avalanche photodetector by exploiting the large Schottky barrier between InSe and Al electrodes.<sup>14</sup> The photocurrent response was extended to near-infrared wavelengths and exhibited a peak at 510 nm. Very recently, by virtue of a self-limited depletion region and a vertical fully depleted channel, Hu et al. realized the ultrafast and highly sensitive self-powered photodetection of 2D layered InSe with the thickness of 110 nm. The device can detect radiation ranging from UV to NIR and possesses a cutoff

wavelength of around 1000 nm, showing a detectivity of  $1.26 \times 10^{13}$  Jones and a response speed of  $\sim 200$  ns at 400 nm.<sup>15</sup>

To overcome the low yield and uncontrollable size of mechanically exfoliated InSe layers, the vapor deposition technique has also been explored for the large-scale synthesis of layered InSe. For instance, Hao et al. reported the wafer-scale synthesis of layered InSe nanosheets by pulsed laser deposition (PLD), showing an optical band gap tuned from 1.26 to 2.20 eV when the thickness decreased to 1 nm. The InSe-based phototransistor showed a broad photoresponse to the wavelengths from UV to NIR, and the maximum responsivity reached 27 A/W under 370 nm illumination.<sup>16</sup> Chen et al. synthesized monolayer InSe with lateral size of approximately several tens of micrometers through the vapor phase reaction of  $\text{In}_2\text{O}_3$  with Se.<sup>17</sup> InSe nanoflakes with tunable thickness have also been successfully realized through a controlled chemical vapor transport (CVT), showing a band gap change from 1.23 to 1.60 eV.<sup>18</sup> According to the evolution of the electronic band structure in few-layered InSe revealed by Lei et al., the blue shift should be ascribed to the suppressed interlayer electron orbital coupling with decreasing number of layers.<sup>19</sup> As the number of layers goes down below  $\sim 7$  layers, the electronic transition from  $p_z$ -like orbitals to the bottom of

**Received:** February 21, 2022

**Accepted:** March 15, 2022

**Published:** March 18, 2022



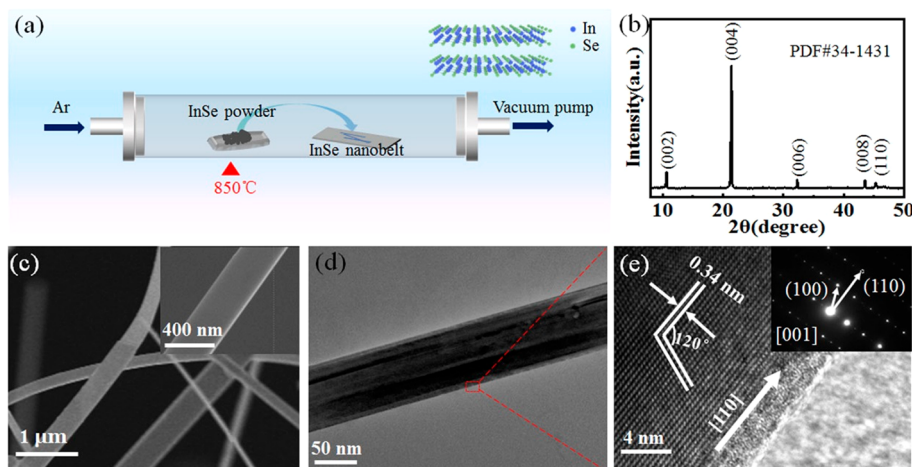


**Figure 1.** (a) Schematic illustration for the synthesis of InSe nanobelt. Characterization of the obtained InSe nanobelts: (b) XRD pattern, (c) FESEM images, (d) TEM image, and (e) HRTEM image. The inset in panel e shows the corresponding SAED pattern.

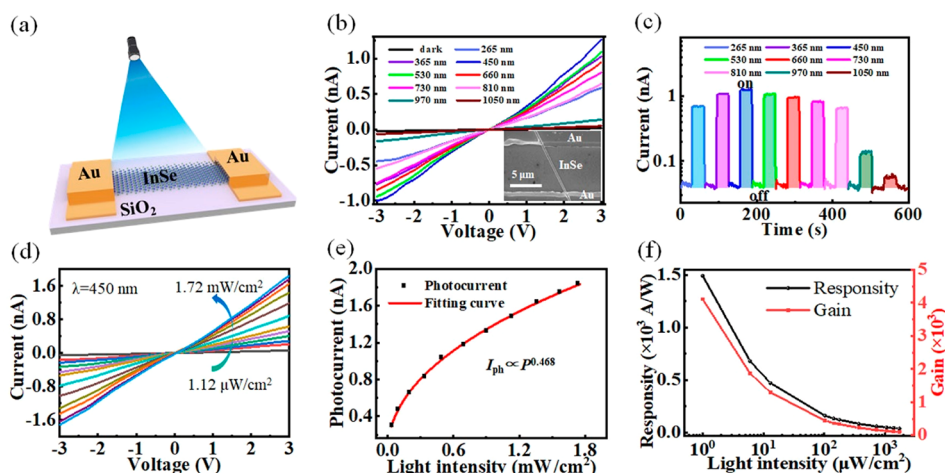


**Figure 2.** (a) Schematic of the InSe nanobelt-based photodetector. (b) Current–voltage ( $I$ – $V$ ) curves of the 165 nm nanobelt photodetector in the dark and upon illumination with different wavelengths at the light intensity of  $0.8 \text{ mW/cm}^2$ . The inset shows the FESEM image of the device. (c) Time-dependent ( $I$ – $T$ ) photoresponse of the device illuminated by incident light with various wavelengths at 3 V bias. (d)  $I$ – $V$  curves of the photodetector upon 450 nm illumination with varied light intensities. (e) The photocurrent as a function of light intensity. (f) Responsivity and gain as a function of light intensity upon 450 nm illumination.

the conduction band (corresponding to the band gap of 1.4 eV) is strongly suppressed while the transition from  $p_{xy}$ -like orbitals to the bottom of the conduction band (corresponding to the band gap of 2.4 eV) does not change appreciably.

Herein, we reported the synthesis of InSe nanobelts through a catalyst-free growth approach in a CVD system, and a blue shift of the photoresponse peak was observed with decreasing the thickness of InSe nanobelt from 562 to 165 nm. Silvaco Technology Computer Aided Design (TCAD) was used to simulate the absorption of incident light within the InSe nanobelt, which revealed that the blue shift of photoresponse peak should be ascribed to the wavelength-dependent absorption coefficient of the InSe crystal.<sup>20</sup> Photodetectors sensitive to blue (450 nm), green (530 nm), and red (660 nm) incident light were obtained, separately, and the spectral reconstruction of a purple “H” has been realized by using the three devices, suggesting the potential application of spectral engineering in full-color imaging.

The InSe nanobelts were synthesized in a horizontal tube furnace by using high-purity InSe powder as the evaporation source (as illustrated in Figure 1a), and more experimental

details can be found in the Supporting Information. Figure 1b presents the X-ray diffraction (XRD) pattern of the as-obtained products. The remarkable diffraction peaks correspond to the crystal planes (002), (004), (006), (008), and (110) of hexagonal InSe (JCPDS No. 34-1431),<sup>21</sup> which suggests a strong preferential orientation along the  $c$ -axis. Field-emission scanning electron microscopy (FESEM) images (Figure 1c) and transmission electron microscopy (TEM) images (Figure 1d) show nanobelt structure with smooth surfaces and high aspect ratios. The width is mostly 400 nm, and the length is up to tens of micrometers. The energy dispersive spectrometry (EDS) spectrum taken from a typical InSe nanobelt is shown in Figure S1, which reveals that the nanobelt mainly consists of indium (In) and selenium (Se) elements. The atomic ratio of In/Se is calculated to be about 1.09, which is very close to the stoichiometry of InSe. Further, the element mapping results shown in Figure S2 reveal the homogeneous distribution of the elements In and Se throughout the whole structure. The high-resolution TEM (HRTEM) image taken from the edge of a single InSe nanobelt is shown in Figure 1e. The well-defined 2D lattice fringes indicate the decent crystallinity of InSe

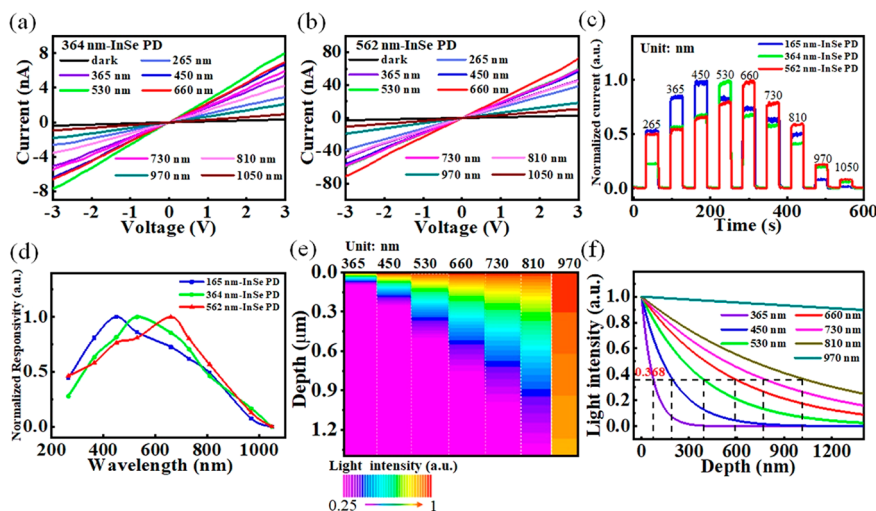


**Figure 3.** (a)  $I$ – $V$  curves of 364 nm InSe nanobelt-based photodetector in the dark and upon illumination with different wavelengths at the light intensity of  $0.8 \text{ mW/cm}^2$ . (b)  $I$ – $V$  curves of 562 nm InSe nanobelt-based photodetector in the dark and upon illumination with different wavelengths at the light intensity of  $0.8 \text{ mW/cm}^2$ . (c) Normalized  $I$ – $T$  curves under illumination with varied wavelengths. (d) Normalized photoresponse of devices based on nanobelts with different thicknesses. (e) The simulated attenuation of light intensity versus depth and (f) the normalized attenuation curve.

nanobelt, and the interplanar spacing of  $0.34 \text{ nm}$  corresponds to the (100) lattice plane of hexagonal InSe. Combining this with the selected area electron diffraction (SAED) pattern (inset in Figure 1e), we can find that the nanobelt grew along the  $[110]$  direction and gave rise to a flat surface parallel to the (001) lattice plane.<sup>22</sup> This is consistent with the layered structure of InSe (Se–In–In–Se layer stacked along  $c$ -axis) and the preferential orientation shown in the XRD pattern (Figure 1b).

In order to study the photoelectrical properties of the InSe nanobelt, a two-terminal device was constructed by using an individual InSe nanobelt as the building block, and the schematic of the device is shown in Figure 2a. A representative SEM image of the device is inset in Figure 2b, and the atomic force microscopy (AFM) image (Figure S3) reveals that the thickness of the InSe nanobelt is about  $165 \text{ nm}$ . Figure 2b plots the current–voltage ( $I$ – $V$ ) curves of the device measured in the dark and upon illumination with different wavelengths at the same intensity ( $0.8 \text{ mW/cm}^2$ ). Apparently, the device shows an excellent photoresponse to a broadband spectrum from  $265$  to  $1050 \text{ nm}$ . The cutoff edge corresponds to the band gap of InSe ( $1.25 \text{ eV}$ ) deduced from the plot of  $(\alpha h\nu)^2 - h\nu$  (shown in Figure S4b). As one can learn from the time-dependent photoresponse shown in Figure 2c, the device can be reversibly turned between low- and high-conductance states with good repeatability. The highest photoresponse exists under  $450 \text{ nm}$  illumination, giving the  $I_{\text{on}}/I_{\text{off}}$  ratio of about 30. Figure 2d shows the  $I$ – $V$  curves of the device under  $450 \text{ nm}$  illumination with different light intensities. It is apparent that the photocurrent increased monotonously from  $0.061$  to  $1.85 \text{ nA}$  when the light intensity rose from  $1.12 \text{ } \mu\text{W/cm}^2$  to  $1.72 \text{ mW/cm}^2$ . The dependence of photocurrent on light intensity can be further fitted with the widely employed power law  $I_{\text{ph}} \sim P^\theta$ , where  $I_{\text{ph}}$  is defined as the net photocurrent ( $I_{\text{ph}} = I_{\text{light}} - I_{\text{dark}}$ ) and  $\theta$  is an empirical value. The  $\theta$  value was fitted to be about  $0.468$ , the deviation of which from the ideal value ( $\theta = 1$ ) indicated the existence of recombination loss in the device.<sup>23,24</sup>

Responsivity ( $R$ ) and gain ( $G$ ) are two key figure-of-merit parameters to quantitatively assess the photodetector performance, which can be calculated by the following equations:<sup>25,26</sup>

$$R = \frac{I_{\text{ph}}}{S P_{\text{in}}} \quad (1)$$

$$G = \frac{hcR}{q\eta\lambda} \quad (2)$$

where  $S$ ,  $P_{\text{in}}$ ,  $h$ ,  $c$ ,  $q$ ,  $\eta$ , and  $\lambda$  represent the effective illumination area (about  $2.58 \times 10^{-8} \text{ cm}^2$  for this device), incident light intensity, Planck constant, velocity of light, electronic charge, internal quantum efficiency, and incident wavelength, respectively. As is shown in Figure 2f, both  $R$  and  $G$  increase gradually as the light intensity declines. This can be attributed to the higher recombination loss upon light irradiation with higher intensity because more carriers are generated. By assuming 100% internal quantum efficiency,  $R$  and  $G$  reached the values of  $1.49 \times 10^3 \text{ A/W}$  and  $4.11 \times 10^3$  at a  $3 \text{ V}$  bias under an intensity of  $1.12 \text{ } \mu\text{W/cm}^2$ , respectively, which are much higher than those of most previously reported InSe devices with a similar structure (shown in Table S1).

To evaluate the ability of the device to detect a weak optical signal, the specific detectivity ( $D^*$ ) was calculated by the noise equivalent power (NEP)<sup>27,28</sup>

$$\text{NEP} = \frac{\overline{i_n^2}^{1/2}}{R} \quad (3)$$

$$D^* = \frac{(S \times \Delta f)^{1/2}}{\text{NEP}} \quad (4)$$

where  $\overline{i_n^2}^{1/2}$  is the root-mean-square value of the noise current and  $\Delta f$  denotes the specific bandwidth. The highest NEP and the highest  $D^*$  were calculated to be  $3.15 \times 10^{-17} \text{ W/Hz}^{1/2}$  and  $5.35 \times 10^{12} \text{ Jones}$ , respectively, showing the ability to detect the weak light signals.

The optoelectronic characteristics of photodetectors based on  $364$  and  $562 \text{ nm}$  InSe nanobelts were further studied and



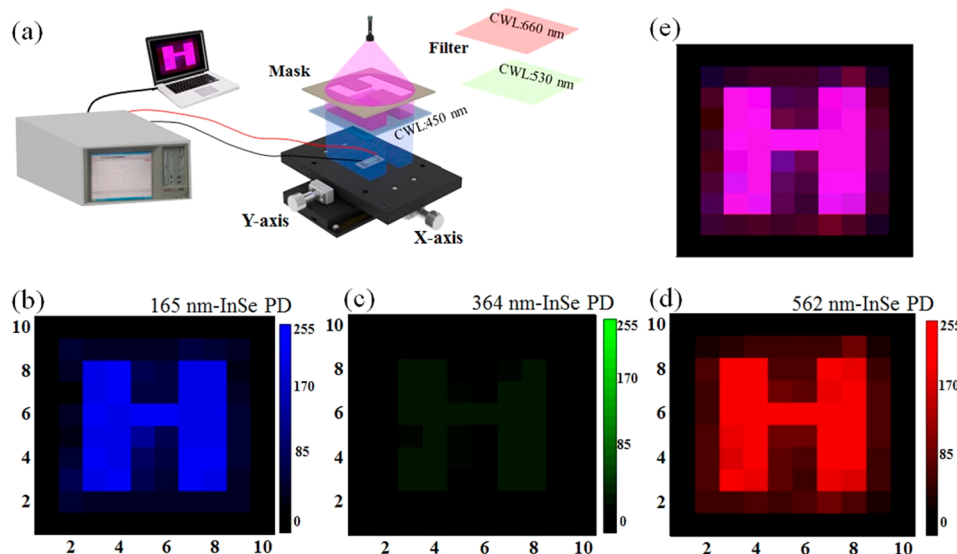


**Figure 4.** (a) Schematic illustration of the visible light imaging system. (b) 2D gray mapping of 165 nm InSe nanobelt-based photodetector upon illumination by using the blue filter. (c) 2D gray mapping of 364 nm InSe nanobelt-based photodetector upon illumination by using the green filter. (d) 2D gray mapping of 562 nm InSe nanobelt-based photodetector upon illumination by using the red filter. (e) Spectral reconstruction of the original purple “H” pattern.

are plotted in Figure 3a–d and Figures S6–S8. Figure 3a depicts the  $I$ – $V$  curves of the 364 nm InSe nanobelt-based photodetector in dark and upon illumination with different wavelengths (light intensity:  $0.8 \text{ mW/cm}^2$ ). We can notice that the device shows a broadband photoresponse to incident light from 265 to 1050 nm, with the highest photocurrent under 530 nm illumination. In addition, for the 562 nm InSe nanobelt-based photodetector, the peak photocurrent is located at 660 nm illumination (Figure 3b). As can be seen from the normalized  $I$ – $T$  curves (Figure 3c) and spectral response (Figure 3d), the peak response of InSe nanobelt-based photodetectors presents an apparent blue shift with decreasing thickness from 562 to 165 nm. The blue shift of the spectrum should not be ascribed to the suppressed interlayer electron orbital coupling because the layers of InSe are far beyond 7.<sup>19</sup> Therefore, the thickness-dependent spectral engineering of layered InSe is still to be systematically studied.

To reveal the thickness-dependent photoresponse of the InSe nanobelt, the photon absorption in InSe crystal upon light illumination with different wavelengths was simulated by Silvaco TCAD. Because of the wavelength-dependent absorption coefficient,<sup>20</sup> the photon absorption in InSe crystal varies for incident light with different wavelengths. As depicted in Figure S9, the photo absorption rate of incident light with short wavelength is relatively large on the surface of InSe crystal because of the high absorption coefficient (shown in Table S2), but it attenuates faster when penetrating into the crystal. According to the normalized attenuation curve of incident light (shown in Figure 3e,f), the penetration depth (defined as the distance where the energy of incident light is reduced to  $1/e$  when it propagates in the medium)<sup>29</sup> for 450 nm incident light is deduced to be approximately 192 nm. With increasing wavelength, the absorption coefficient decreases greatly, giving rise to a lower photon absorption rate on the surface and a larger penetration depth (approximately 384 nm for 530 nm incident light and 581 nm for 660 nm incident light, respectively). This well explains the blue shift of photoresponse with decreasing thickness of

the InSe nanobelt shown in Figure 3d. Within the 165 nm InSe nanobelt, the attenuation of 450 nm incident light reaches approximately 57.4%, which is only approximately 34.7% for 530 nm incident light and 24.5% for 660 nm incident light. The higher photon absorption rate will bring about more photogenerated carriers in the semiconductor, leading to a higher photocurrent at 450 nm. When the thickness of the InSe nanobelt increases to 364 nm, both 450 and 530 nm incident light could be completely absorbed, leading to the red shift of the peak photoresponse. However, the photocurrent under 450 nm illumination is slightly decreased, which may be ascribed to the higher surface recombination arising from the inevitable defects and surface states.<sup>30</sup> Notably, the thickness-dependent spectral engineering has also been observed in many 2D layered semiconductors, such as two-dimensional transition metal dichalcogenide (TMDC)  $\text{MoS}_2$ <sup>31</sup> and 2D perovskites.<sup>32</sup>

Inspired by the thickness-dependent spectral engineering of InSe nanobelt-based photodetector, we then explored the potential application in the full-color imaging using the setup shown in Figure 4a. A polychromatic purple light-emitting diode (LED) was used as the light source, and a lab-built mask ( $5 \text{ cm} \times 5 \text{ cm}$ ) with a hollow pattern of “H” was placed under it to obtain a color image. Color filters with central wavelength (CWL) of 660 nm (red filter), 530 nm (green filter), and 450 nm (blue filter) were used to obtain RGB signals, and the devices based on 562, 364, and 165 nm InSe nanobelts were adopted to detect the R, G, and B signals, respectively. The devices were fixed on an automatic displacement system to progressively scan horizontally ( $x$ -axis) and vertically ( $y$ -axis), and the photocurrent of every spot was recorded. The photocurrents were normalized by the maximum photocurrents of the corresponding RGB pixels for full-color image processing and converted into corresponding gray values (from 0 to 255),<sup>33</sup> which were then incorporated into the 2D gray mappings (shown in Figure 4b–d). Through combination of the three different color images, a composite color image (a purple “H” pattern) could be obtained (Figure 4e). Clearly,

any color visible light could be detected by this way. This indicates that the full-color imaging can be realized by the thickness-dependent spectral engineering of 2D layered semiconductors.

In conclusion, we have demonstrated the fabrication of photodetectors with tunable spectral response by utilizing InSe nanobelts with different thickness as the building blocks. Because of the wavelength-dependent absorption coefficient of InSe, incident light with shorter wavelengths are absorbed near the surface while longer-wavelength light has a larger penetration depth, leading to a blue-shift of the peak photoresponse for InSe nanobelt-based photodetector with decreasing thickness. Photodetectors sensitive to blue, green, and red incident light were obtained, which enables the spectral reconstruction of a purple “H” pattern. This provides a simple and effective method for spectral engineering and indicates the potential application of 2D layered semiconductors in full-color imaging.

## ■ ASSOCIATED CONTENT

### SI Supporting Information

The Supporting Information is available free of charge at <https://pubs.acs.org/doi/10.1021/acs.jpclett.2c00518>.

Details for preparation and characterization of InSe nanobelts and InSe nanobelts-based photodetectors, theoretical simulation, EDS spectrum and elemental mapping of a typical InSe nanobelt, height profile of InSe nanobelts and corresponding AFM images, absorption spectrum of as-obtained InSe nanobelts and the plot of  $(\alpha h\nu)^2$  versus photon energy ( $h\nu$ ), dark current of 165 nm InSe nanobelt-based photodetector and the noise spectral density based on the Fourier transform of the dark current, optoelectronic characterization of 364 nm and 562 nm InSe nanobelt-based photodetector, simulated photon absorption rate versus depth in InSe crystal, comparison of key parameters between our work and other previously reported InSe-based photodetectors with similar structures, and absorption coefficient and calculated penetration depth for light with different wavelengths (PDF)

## ■ AUTHOR INFORMATION

### Corresponding Authors

**Chun-Yan Wu** – School of Microelectronics, Hefei University of Technology, Hefei 230009, China; [orcid.org/0000-0001-5793-6772](https://orcid.org/0000-0001-5793-6772); Email: [cywu@hfut.edu.cn](mailto:cywu@hfut.edu.cn)

**Lin-Bao Luo** – School of Microelectronics, Hefei University of Technology, Hefei 230009, China; [orcid.org/0000-0001-8651-8764](https://orcid.org/0000-0001-8651-8764); Email: [luolb@hfut.edu.cn](mailto:luolb@hfut.edu.cn)

### Authors

**Kai-Jun Cao** – School of Microelectronics, Hefei University of Technology, Hefei 230009, China

**Yu-Xuan Le** – School of Microelectronics, Hefei University of Technology, Hefei 230009, China

**Jing-Yue Li** – School of Microelectronics, Hefei University of Technology, Hefei 230009, China

**Chen-Yue Zhu** – School of Microelectronics, Hefei University of Technology, Hefei 230009, China

**Li Wang** – School of Microelectronics, Hefei University of Technology, Hefei 230009, China; [orcid.org/0000-0002-9125-7447](https://orcid.org/0000-0002-9125-7447)

**Yu-Xue Zhou** – College of Physical Science and Technology, Yangzhou University, Yangzhou 225002, China  
**Di Wu** – Key Laboratory of Materials Physics of Ministry of Education, Department of Physics and Engineering, Zhengzhou University, Zhengzhou 450052, China; [orcid.org/0000-0003-3266-0612](https://orcid.org/0000-0003-3266-0612)

Complete contact information is available at: <https://pubs.acs.org/doi/10.1021/acs.jpclett.2c00518>

## Notes

The authors declare no competing financial interest.

## ■ ACKNOWLEDGMENTS

This work is supported by the National Natural Science Foundation of China (Nos. 62074048 and 51902078), the Natural Science Foundation of Anhui Province (No. 2108085MF229), and the Fundamental Research Funds for the Central Universities (PA2020GDKC0014).

## ■ REFERENCES

- (1) Tan, C.; Lai, Z.; Zhang, H. Ultrathin Two-Dimensional Multilayered Metal Chalcogenide Nanomaterials. *Adv. Mater.* **2017**, *29*, 1701392.
- (2) Wang, H.; Li, Z.; Li, D.; Chen, P.; Pi, L.; Zhou, X.; Zhai, T. Van der Waals Integration Based on Two-Dimensional Materials for High-Performance Infrared Photodetectors. *Adv. Funct. Mater.* **2021**, *31*, 2103106.
- (3) Buscema, M.; Island, J. O.; Groenendijk, D. J.; Blanter, S. I.; Steele, G. A.; van der Zant, H. S. J.; Castellanos-Gomez, A. Photocurrent Generation with Two-Dimensional van der Waals Semiconductors. *Chem. Soc. Rev.* **2015**, *44*, 3691–3718.
- (4) Coleman, J. N.; Lotya, M.; O'Neill, A.; Bergin, S. D.; King, P. J.; Khan, U.; Young, K.; Gaucher, A.; De, S.; Smith, R. J.; et al. Two-dimensional Nanosheets Produced by Liquid Exfoliation of Layered Materials. *Science* **2011**, *331*, 568–571.
- (5) Song, C.; Noh, G.; Kim, T. S.; Kang, M.; Song, H.; Ham, A.; Jo, M. K.; Cho, S.; Chai, H. J.; Cho, S. R.; et al. Growth and Interlayer Engineering of 2D Layered Semiconductors for Future Electronics. *ACS Nano* **2020**, *14*, 16266–16300.
- (6) Xu, M.; Liang, T.; Shi, M.; Chen, H. Graphene-Like Two-dimensional Materials. *Chem. Rev.* **2013**, *113*, 3766–3798.
- (7) Peng, B.; Ang, P. K.; Loh, K. P. Two-dimensional Dichalcogenides for Light-Harvesting Applications. *Nano Today* **2015**, *10*, 128–137.
- (8) Shim, J.; Park, H.-Y.; Kang, D.-H.; Kim, J.-O.; Jo, S.-H.; Park, Y.; Park, J.-H. Electronic and Optoelectronic Devices Based on Two-Dimensional Materials: From Fabrication to Application. *Adv. Electron. Mater.* **2017**, *3*, 1600364.
- (9) Huang, W.; Gan, L.; Li, H.; Ma, Y.; Zhai, T. 2D Layered Group IIIA Metal Chalcogenides: Synthesis, Properties and Applications in Electronics and Optoelectronics. *CrystEngComm* **2016**, *18*, 3968–3984.
- (10) Li, M.; Lin, C.-Y.; Yang, S.-H.; Chang, Y.-M.; Chang, J.-K.; Yang, F.-S.; Zhong, C.; Jian, W.-B.; Lien, C.-H.; Ho, C.-H.; et al. High Mobilities in Layered InSe Transistors with Indium-Encapsulation-Induced Surface Charge Doping. *Adv. Mater.* **2018**, *30*, 1803690.
- (11) Mudd, G. W.; Svatek, S. A.; Ren, T.; Patané, A.; Makarovskiy, O.; Eaves, L.; Beton, P. H.; Kovalyuk, Z. D.; Lashkarev, G. V.; Kudrynskiy, Z. R.; et al. Tuning the Bandgap of Exfoliated InSe Nanosheets by Quantum Confinement. *Adv. Mater.* **2013**, *25*, 5714–5718.
- (12) Dai, M.; Chen, H.; Wang, F.; Hu, Y.; Wei, S.; Zhang, J.; Wang, Z.; Zhai, T.; Hu, P. Robust Piezo-Phototronic Effect in Multilayer  $\gamma$ -InSe for High-Performance Self-Powered Flexible Photodetectors. *ACS Nano* **2019**, *13*, 7291–7299.

- (13) Tamalampudi, S. R.; Lu, Y.-Y.; Kumar, U. R.; Sankar, R.; Liao, C.-D.; Moorthy, B. K.; Cheng, C.-H.; Chou, F. C.; Chen, Y.-T. High Performance and Bendable Few-Layered InSe Photodetectors with Broad Spectral Response. *Nano Lett.* **2014**, *14*, 2800–2806.
- (14) Lei, S.; Wen, F.; Ge, L.; Najmaei, S.; George, A.; Gong, Y.; Gao, W.; Jin, Z.; Li, B.; Lou, J.; et al. An Atomically Layered InSe Avalanche Photodetector. *Nano Lett.* **2015**, *15*, 3048–3055.
- (15) Dai, M.; Chen, H.; Wang, F.; Long, M.; Shang, H.; Hu, Y.; Li, W.; Ge, C.; Zhang, J.; Zhai, T.; et al. Ultrafast and Sensitive Self-Powered Photodetector Featuring Self-Limited Depletion Region and Fully Depleted Channel with van der Waals Contacts. *ACS Nano* **2020**, *14*, 9098–9106.
- (16) Yang, Z.; Jie, W.; Mak, C.-H.; Lin, S.; Lin, H.; Yang, X.; Yan, F.; Lau, S. P.; Hao, J. Wafer-Scale Synthesis of High-Quality Semi-conducting Two-Dimensional Layered InSe with Broadband Photo-response. *ACS Nano* **2017**, *11*, 4225–4236.
- (17) Chang, H.-C.; Tu, C.-L.; Lin, K.-I.; Pu, J.; Takenobu, T.; Hsiao, C.-N.; Chen, C.-H. Synthesis of Large-Area InSe Monolayers by Chemical Vapor Deposition. *Small* **2018**, *14*, 1802351.
- (18) Yuan, K.; Yin, R.; Li, X.; Han, Y.; Wu, M.; Chen, S.; Liu, S.; Xu, X.; Watanabe, K.; Taniguchi, T.; et al. Realization of Quantum Hall Effect in Chemically Synthesized InSe. *Adv. Funct. Mater.* **2019**, *29*, 1904032.
- (19) Lei, S.; Ge, L.; Najmaei, S.; George, A.; Kappera, R.; Lou, J.; Chhowalla, M.; Yamaguchi, H.; Gupta, G.; Vajtai, R.; et al. Evolution of the Electronic Band Structure and Efficient Photo-Detection in Atomic Layers of InSe. *ACS Nano* **2014**, *8*, 1263–1272.
- (20) Sang, D. K.; Wang, H.; Qiu, M.; Cao, R.; Guo, Z.; Zhao, J.; Li, Y.; Xiao, Q.; Fan, D.; Zhang, H. Two Dimensional  $\beta$ -InSe with Layer-Dependent Properties: Band Alignment, Work Function and Optical Properties. *Nanomaterials* **2019**, *9*, 82.
- (21) Feng, W.; Zheng, W.; Cao, W.; Hu, P. Back Gated Multilayer InSe Transistors with Enhanced Carrier Mobilities via the Suppression of Carrier Scattering from a Dielectric Interface. *Adv. Mater.* **2014**, *26*, 6587–6593.
- (22) Dai, M.; Chen, H.; Feng, R.; Feng, W.; Hu, Y.; Yang, H.; Liu, G.; Chen, X.; Zhang, J.; Xu, C.-Y.; et al. A Dual-Band Multilayer InSe Self-Powered Photodetector with High Performance Induced by Surface Plasmon Resonance and Asymmetric Schottky Junction. *ACS Nano* **2018**, *12*, 8739–8747.
- (23) Zeng, L.-H.; Lin, S.-H.; Li, Z.-J.; Zhang, Z.-X.; Zhang, T.-F.; Xie, C.; Mak, C.-H.; Chai, Y.; Lau, S. P.; Luo, L.-B.; et al. Self-Driven, Air-Stable, and Broadband Photodetector Based on Vertically Aligned PtSe<sub>2</sub>/GaAs Heterojunction. *Adv. Funct. Mater.* **2018**, *28*, 1705970.
- (24) Wang, L.; Jie, J.; Shao, Z.; Zhang, Q.; Zhang, X.; Wang, Y.; Sun, Z.; Lee, S.-T. MoS<sub>2</sub>/Si Heterojunction with Vertically Standing Layered Structure for Ultrafast, High-Detectivity, Self-Driven Visible-Near Infrared Photodetectors. *Adv. Funct. Mater.* **2015**, *25*, 2910–2919.
- (25) Li, J.; Niu, L.; Zheng, Z.; Yan, F. Photosensitive Graphene Transistors. *Adv. Mater.* **2014**, *26*, 5239–5273.
- (26) Xie, C.; Liu, C.-K.; Loi, H.-L.; Yan, F. Perovskite-Based Phototransistors and Hybrid Photodetectors. *Adv. Funct. Mater.* **2020**, *30*, 1903907.
- (27) Xie, C.; Mak, C.; Tao, X.; Yan, F. Photodetectors Based on Two-Dimensional Layered Materials Beyond Graphene. *Adv. Funct. Mater.* **2017**, *27*, 1603886.
- (28) Liu, X.; Gu, L.; Zhang, Q.; Wu, J.; Long, Y.; Fan, Z. All-printable Band-Edge Modulated ZnO Nanowire Photodetectors with Ultra-High Detectivity. *Nat. Commun.* **2014**, *5*, 4007.
- (29) Chen, C.; Mou, F.; Xu, L.; Wang, S.; Guan, J.; Feng, Z.; Wang, Q.; Kong, L.; Li, W.; Wang, J.; et al. Light-Steered Isotropic Semiconductor Micromotors. *Adv. Mater.* **2017**, *29*, 1603374.
- (30) Zhao, Q.; Wang, W.; Carrascoso-Plana, F.; Jie, W.; Wang, T.; Castellanos-Gomez, A.; Frisenda, R. The Role of Traps in the Photocurrent Generation Mechanism in Thin InSe Photodetectors. *Mater. Horiz.* **2020**, *7*, 252–262.
- (31) Das, S.; Chen, H.-Y.; Penumatcha, A. V.; Appenzeller, J. High Performance Multilayer MoS<sub>2</sub> Transistors with Scandium Contacts. *Nano Lett.* **2013**, *13*, 100–105.
- (32) Li, Z.; Hong, E.; Zhang, X.; Deng, M.; Fang, X. Perovskite-Type 2D Materials for High-Performance Photodetectors. *J. Phys. Chem. Lett.* **2022**, *13*, 1215–1225.
- (33) Lan, Z.; Zhu, F. Electrically Switchable Color-Selective Organic Photodetectors for Full-Color Imaging. *ACS Nano* **2021**, *15*, 13674–13682.